Supplemental Material: Negative electronic compressibility in charge islands in twisted bilayer graphene

Robin J. Dolleman,[1,*] Alexander Rothstein,[1,2] Ammon Fischer,[3] Lennart Klebl,[4] Lutz Waldecker,[1] Kenji Watanabe,[5] Takashi Taniguchi,[6] Dante M. Kennes,[3,7] Florian Libisch,[8] Bernd Beschoten,[1] and Christoph Stampfer[1,2,†]

[1] *JARA-FIT and 2nd Institute of Physics, RWTH Aachen University, 52074 Aachen, Germany, EU*
[2] *Peter Grünberg Institute (PGI-9), Forschungszentrum Jülich, 52425 Jülich, Germany, EU*
[3] *JARA-FIT and Institut für Theorie der Statistischen Physik, RWTH Aachen University, 52074 Aachen, Germany, EU*
[4] *I. Institute of Theoretical Physics, University of Hamburg, Notkestrasse 9, 22607 Hamburg, Germany, EU*
[5] *Research Center for Functional Materials, National Institute for Materials Science, 1-1 Namiki, Tsukuba 305-0044, Japan*
[6] *International Center for Materials Nanoarchitectonics, National Institute for Materials Science, 1-1 Namiki, Tsukuba 305-0044, Japan*
[7] *Max Planck Institute for the Structure and Dynamics of Matter, Center for Free Electron Laser Science, Hamburg, Germany, EU*
[8] *Institute for Theoretical Physics, Vienna University of Technology, 1040 Vienna, Austria, EU*

CONTENTS

* dolleman@physik.rwth-aachen.de

† stampfer@physik.rwth-aachen.de

S1. ADDITIONAL BULK TRANSPORT DATA ON THE 750 NM CONSTRICTION

A. Fragile superconductivity in the 750 nm constriction

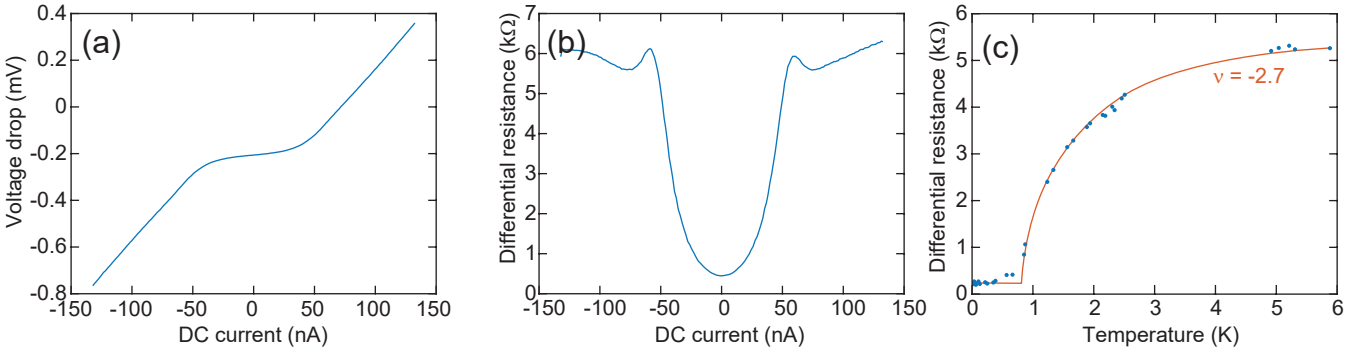

FIG. S1. Observation of fragile superconductivity in constriction C1. (a) Temperature dependence of the 4-point resistance, showing correlated insulators (CI), band insulators (BI) and the fragile superconducting dome (SC). (b) DC voltage drop and (c) differential resistance measured over the 750 nm constriction as a function of DC current. (d) Temperature dependence of the resistance at a filling factor $\nu = -2.7$. Red solid line is a guide to the eye.

In Figs. 1(d)-1(e) of the main text we show the 4-point resistance measured in constriction C1 as a function of temperature. Besides band insulators (BI) and correlated insulators (CI), we find a region with low resistance near $\nu = -2.7$ at low temperatures, resembling a superconducting dome that is often observed in magic angle tBLG. To investigate this further, we measured the voltage-current characteristic at a backgate voltage of -2.43 V and base temperature. Figure S1 shows the DC voltage drop [Fig. S1(a)] and differential resistance [Fig. S1(b)] as a function of DC current. DC signals were simultaneously obtained with AC signals (to obtain the differential resistance) using standard lockin techniques at a frequency of 19.11 Hz. We observe a plateau in the voltage drop around zero DC current and two maxima in the differential resistance. Both are characteristic features of superconductivity, however, a 400 Ω resistance remains. The temperature-dependence of the differential resistance shows a characteristic drop as the temperature decreases, below which it shows a plateau at a finite resistance [Fig. S1(c)]. Therefore, we conclude that we do not observe robust superconductivity as often observed in tBLG [1], but rather a fragile superconducting dome. This may be attributed to a resistance in series to a superconducting region in the 750 nm constriction. Alternatively, the rather large voltage offset of the differential amplifier of 0.2 mV [Fig. S1(a)] might also be responsible for breaking the superconducting state, if this is indeed an offset on the input of the amplifier.

B. Chern insulators in the 750 nm constriction

Figure S2 shows the longitudinal (R_{xx}) and transverse (R_{xy}) resistance as a function of normalized density and flux. These normalized quantities were found by calculating the supercell area from the superlattice density. This directly gives the normalized density, which is equivalent to the number of charge carriers per supercell. The flux through one supercell is normalized with respect to the flux quantum.

As shown in Fig. S2(c) we observe a series of Chern insulators, whose topological invariants are (s, t), where s is the slope and t is the offset. These states are only included in Fig. S2(c) if $R_{xy} = 1/s$ $[h/e^2]$. They have been observed with the same topological invariants in other works in tBLG near the magic angle [2–7] and arise from the energy spectrum of the circular orbits of the charge carriers in the periodic potential of the moiré superlattice.

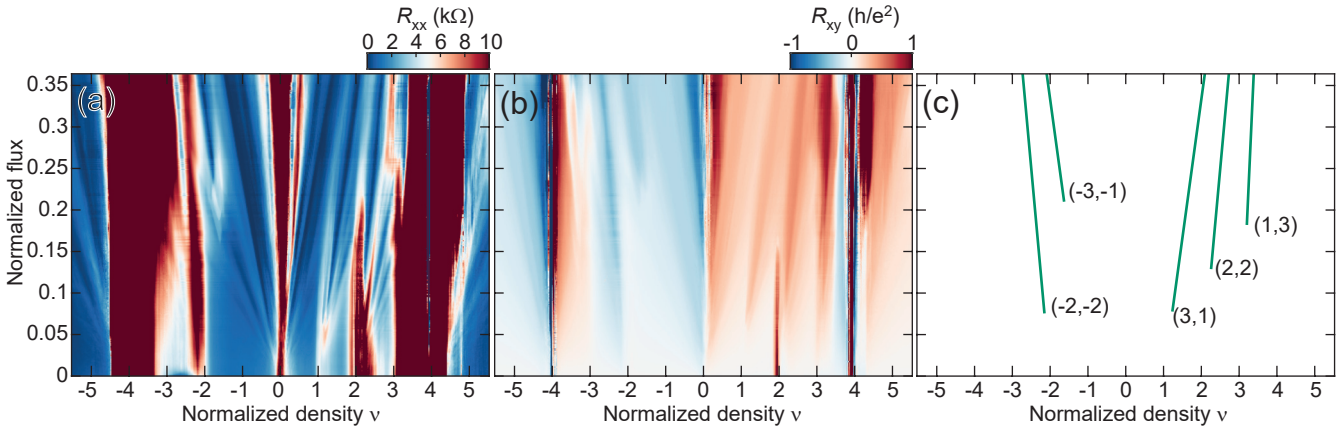

FIG. S2. Observation of Chern insulators in constriction C1. (a) Longitudinal resistance as a function of normalized density $\nu = nA_{\mathrm{uc}}$ and normalized flux Φ/Φ_0. (b) Transverse resistance in units of h/e^2. (c) Wannier diagram of observed Chern insulators

S2. DEPENDENCE OF THE COULOMB OSCILLATIONS ON THE SAMPLE WIDTH

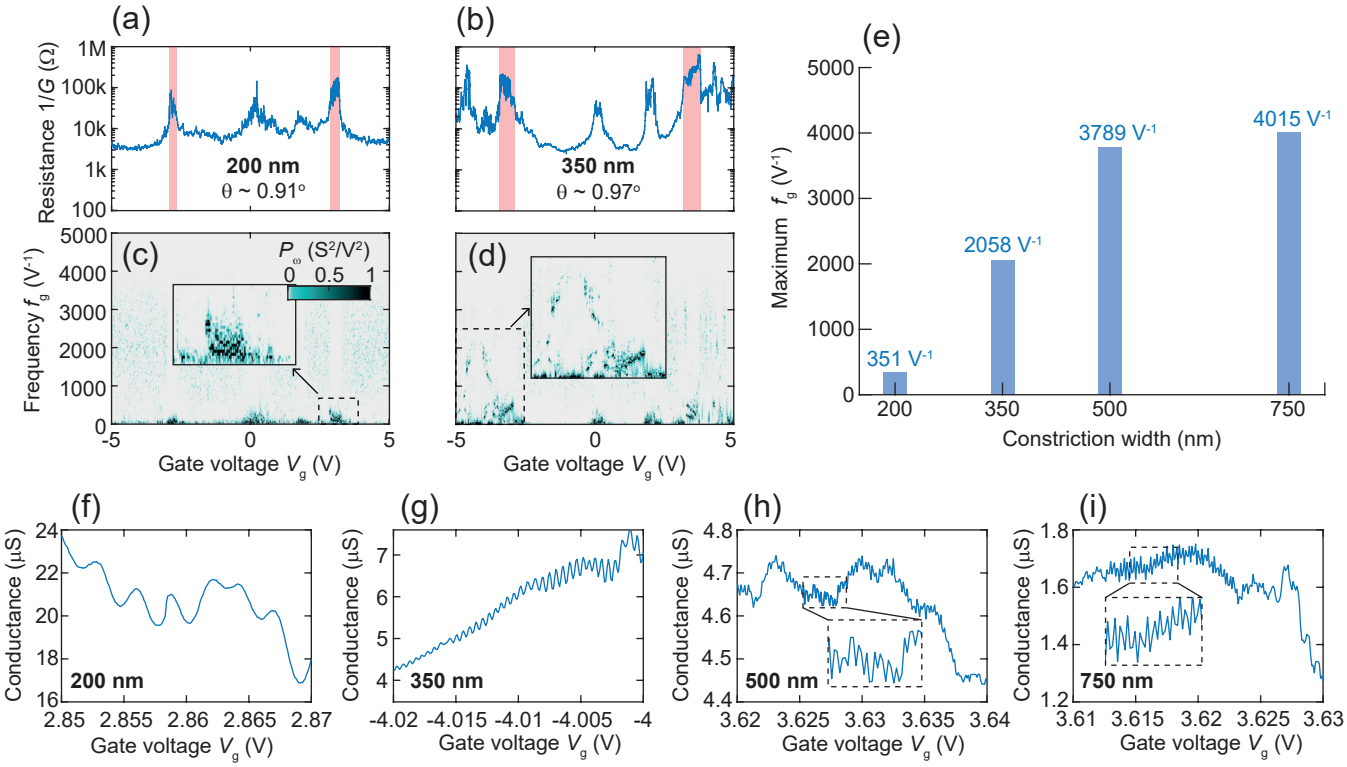

FIG. S3. (a),(b) 2-point conductance traces over the full gate voltage range for the 350 and 200 nm wide constriction, respectively. The band insulators (BI) are highlighted by red shaded regions. (c)–(d) Power spectra P_ω as a function of gate voltage for the 350 and 200 nm wide constriction, respectively. (e) The highest discernible periodic oscillation frequency as a function of constriction width. (f-i) Examplary conductance traces in a 20 mV window for the 200, 350, 500 and 750 nm wide constriction, respectively.

To elucidate the location on the sample where these confinements are formed, we analyze conductance traces taken over each constriction in device D1. Two example traces on the 200 nm and 350 nm wide constriction are shown in Figs. S3(a), S3(b), respectively. To qualitatively evaluate the frequency content within each constriction, we examine the power spectra of each in Figs. 2(b), S3(c), S3(d) (for the 500 nm wide constriction, see section S4), identifying the highest confidently discernible periodic oscillation frequency in each case. This analysis reveals a diminishing trend of high-frequency contributions with decreasing sample width, as visually depicted in Figs. S3(e). Specifically, at a sample width of 200 nm, no high-frequency Coulomb oscillations are evident [Fig. S3(c)], whereas at a width of 350 nm, distinct periodic components are still observable up to 2058 V^{-1} [Fig. S3(d)]. To further illustrate the frequency content within each constriction, we present exemplary traces of the conductance within a 20 mV gate voltage span (close to the maximum in frequency), showcased in Figs. S3(f)–(i).

S3. FITTING RESULTS TO DETERMINE S

TABLE S1. Fitting results on the frequency components with S as a fitting parameter.

Component	Near filling	$\sqrt{A}$	V_0	S	R^2
C1.1	-4	307.4 ± 12.0	-3.909 ± 0.047	1.09 ± 0.13	0.986
C1.2	-4	126.2 ± 10.7	- 3.559 ± 0.118	0.90 ± 0.30	0.911
C1.3	+4	341.8 ± 24.3	3.600 ± 0.040	0.57 ± 0.17	0.987
C1.4	+4	162.7 ± 12.5	3.834 ± 0.016	0.48 ± 0.12	0.950
C2.1	-4	259.6 ± 31.0	-3.605 ± 0.378	2.09 ± 0.60	0.974
C2.5	+4	153.9 ± 13.0	3.797 ± 0.021	0.62 ± 0.13	0.946
C3.2	-4	342.1 ± 44.5	-4.166 ± 0.102	0.69 ± 0.35	0.985
D2.1	-4	119.0 ± 12.7	-4.653 ± 0.052	1.21 ± 0.23	0.977
D2.2	-4	201.0 ± 22.4	-3.968 ± 0.075	0.92 ± 0.30	0.943
D2.3	-4	231.5 ± 70.5	-5.431 ± 0.861	2.70 ± 1.49	0.963
D2.4	+2	301.9 ± 7.9	2.758 ± 0.070	1.05 ± 0.16	0.978
D3.3	+3	216.7 ± 34.0	4.276 ± 0.244	2.50 ± 0.36	0.974

S4. REMAINING PLOTS OF THE OBSERVED FREQUENCY COMPONENTS AND FITS WITH $S = 0.84$

Figure S4 shows the frequency components found near the band insulators on the electron side in sample C1. Component C1.3 is interesting, because the capacitance is lower than expected from our model at low densities. While the cause is unknown, it may be related to the large average distance a exceeding the thickness of the hBN d, causing a significant change in the dielectric screening. It could also be the combined effect of two distinct charge islands with similar sizes, but different V_0. These deviations are not observed in any other frequency component.

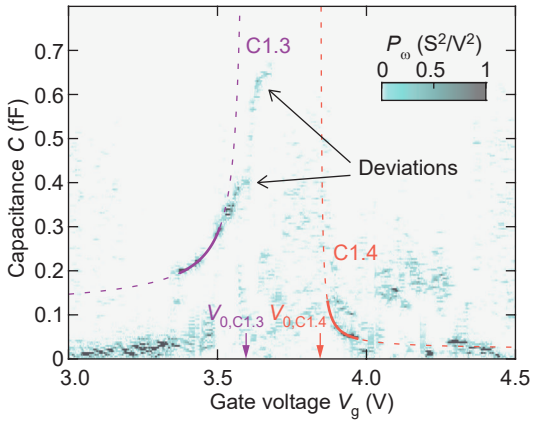

FIG. S4. Frequency components observed on the electron-side in the 750-nm-wide constriction (C1) on sample D1 and fits using Eq. (5).

Figure S5(a) shows the 2 point conductance G as a function of gate voltage over the 500 nm constriction (C2) in device 1. The band insulators are found at different gate voltages than for the 750 nm constriction. This may be attributed to a slight change in twist angle. From the shift in the position of the band insulator we estimate the twist angle to be $\sim 1.07°$. We observe several frequency components near the band insulating features in Fig. S5(b). In Figs. S5(c)–S5(f) we identify 5 components that fit well to Eq. (5).

Figure S6 shows the fits for the 350 nm wide constriction (C3) on device 1. In this region, the twist angle is found to be lower than for the 750 nm constriction. Based on the position of the band insulators, we estimate the twist angle in this region to be $\sim 0.97°$.

Figure S7(a) shows an optical image of sample D2, which consists of a 1 μm-wide Hall bar with an estimated twist angle of 0.97°. In the experiment, we measured the conductance along the total length of the device, using the two contacts indicated by black arrows in Fig. S7(a). We find the frequency components near $\nu = -4$ [Figs. S7(e), S7(f), S7(h), S7(i)] and near $\nu = 2$ [Figs. S7(g), S7(j)] on this sample. Near the band insulator at $\nu = -4$, initially we find two components denoted D2.1 and D2.2 as shown in Figs. S7(c), S7(e), S7(h). To break the insulating state somewhat, we repeated the measurements with an additional 0.5 mV DC bias applied to the sample [Figs. S7(d), S7(f), S7(i)]. This reveals an additional frequency component D2.3 in a region that was previously masked by the insulating state.

Sample D3 consists of a Hall bar structure, however only in one of the contacts the graphene was found to be twisted [bottom contact indicated by a black arrow in Fig. S8(a)], while in the remainder of the sample no moiré-induced satellites are found. When measuring the 2-point conductance [Fig. S8(b)], we find the band insulators and correlated insulators at fractional fillings. Near the band insulators, we find two distinct frequency components near $\nu = -4$ [Figs. S8(d), S8(g)]. We fit only to one component D3.1 [Fig. S8(c)], because the other component is not fully captured in the gate voltage trace which makes it difficult to find V_0 from the fit. During the Landau fan measurement to extract the density, the sample broke, meaning that only data between 7 and 9 T could be used to estimate the lever arm.

In sample D3, the conductance oscillations are prominently visible in a 4-point measurement if this contact is used as a voltage probe due to the oscillating contact resistance. Due to the larger amplitude, this 4-point measurement is used to detect the oscillations in Fig. S8.

In Table S2 we summarize the fitting results of all the frequency components found near the band insulators.

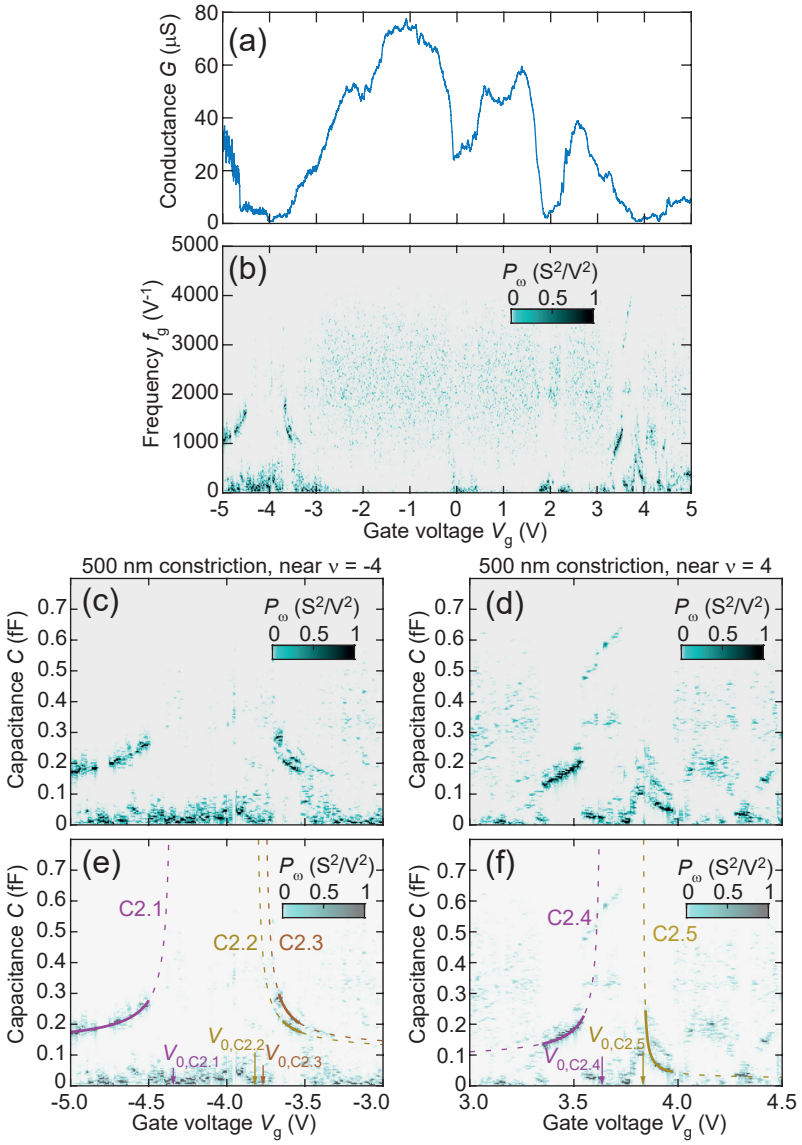

FIG. S5. Frequency components observed in the 500 nm constriction (C2). (a) 2-point conductance as a function of gate voltage. (b) Power spectrum as a function of gate voltage and gate-voltage-frequency over the whole gate voltage range. (c) Power spectrum close to the band insulator on the hole-side and (e) fit to 3 frequency components. (d) Power spectrum close to the band insulator on the electron side and (f) fit to two frequency components.

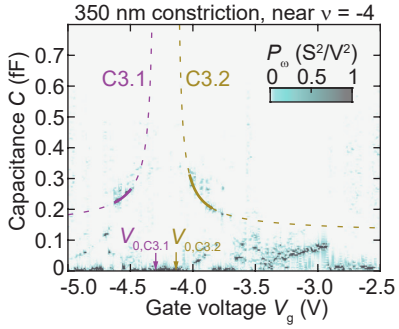

FIG. S6. Power spectrum and fit to two frequency components observed in the 350-nm-wide constriction (C3).

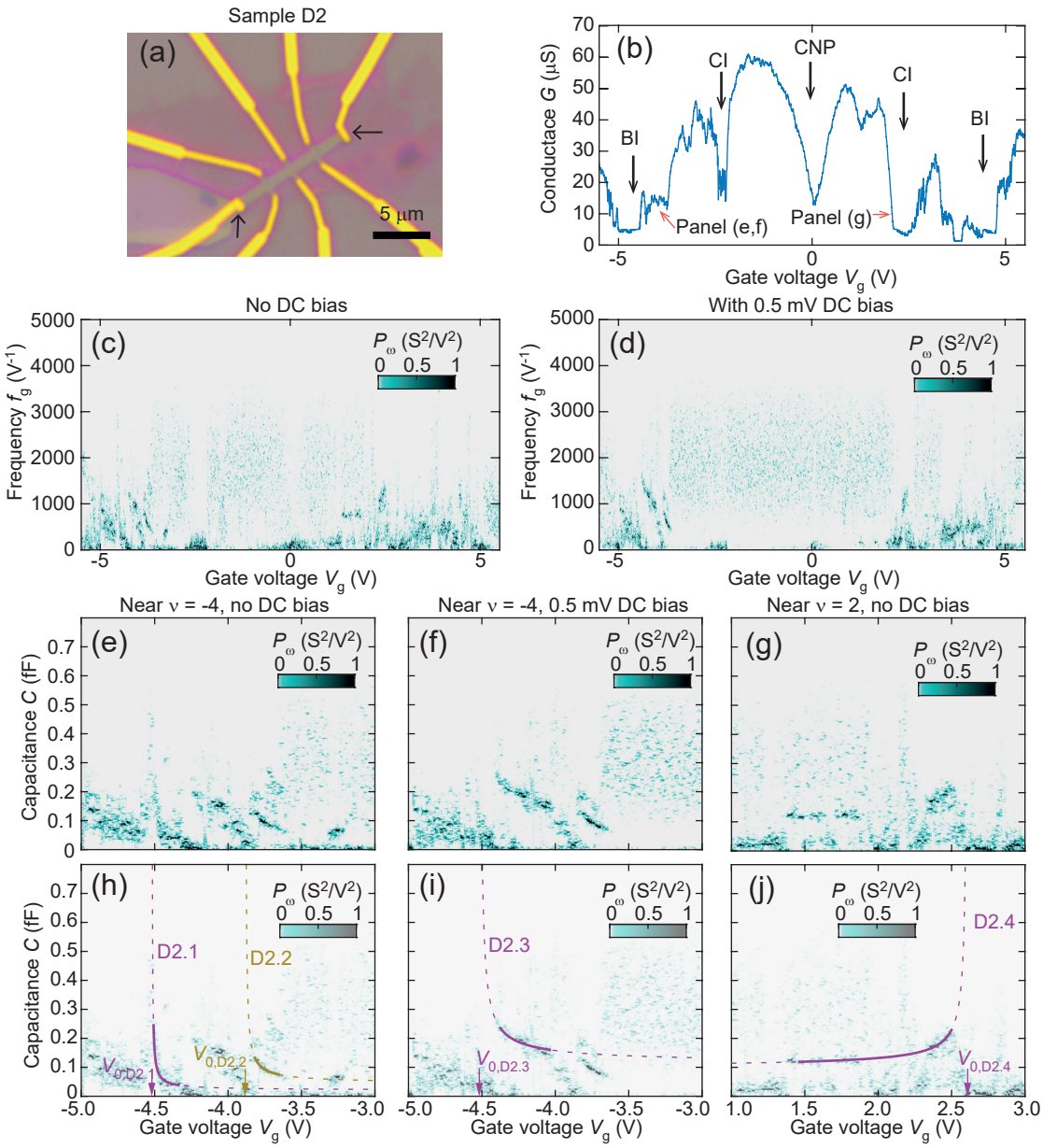

FIG. S7. Conductance oscillations observed in device D2. This sample consists of a simple Hall-bar structure (no constrictions) and tBLG with an estimated twist angle of 0.97°. (a) Optical microscopy image of the device, the two contacts highlighted by black arrows are used for the conductance measurement. (b) Two-point conductance as a function of gate voltage, highlighting the band insulators (BI) and correlated insulators (CI). (c) Power spectrum as a function of gate voltage and frequency without a DC bias applied and (d) with a 0.5 mV DC bias applied. (e) Zoom-in of the Power spectrum as a function of gate voltage and capacitance near the band insulator on the hole-side and (h) including fits to two frequency components. (f) Power spectrum near the band insulator on the hole side with a 0.5 mV bias and (i) fit to an additional frequency component. (g) Power spectrum near half-filling on the hole side and (j) fit to the frequency component.

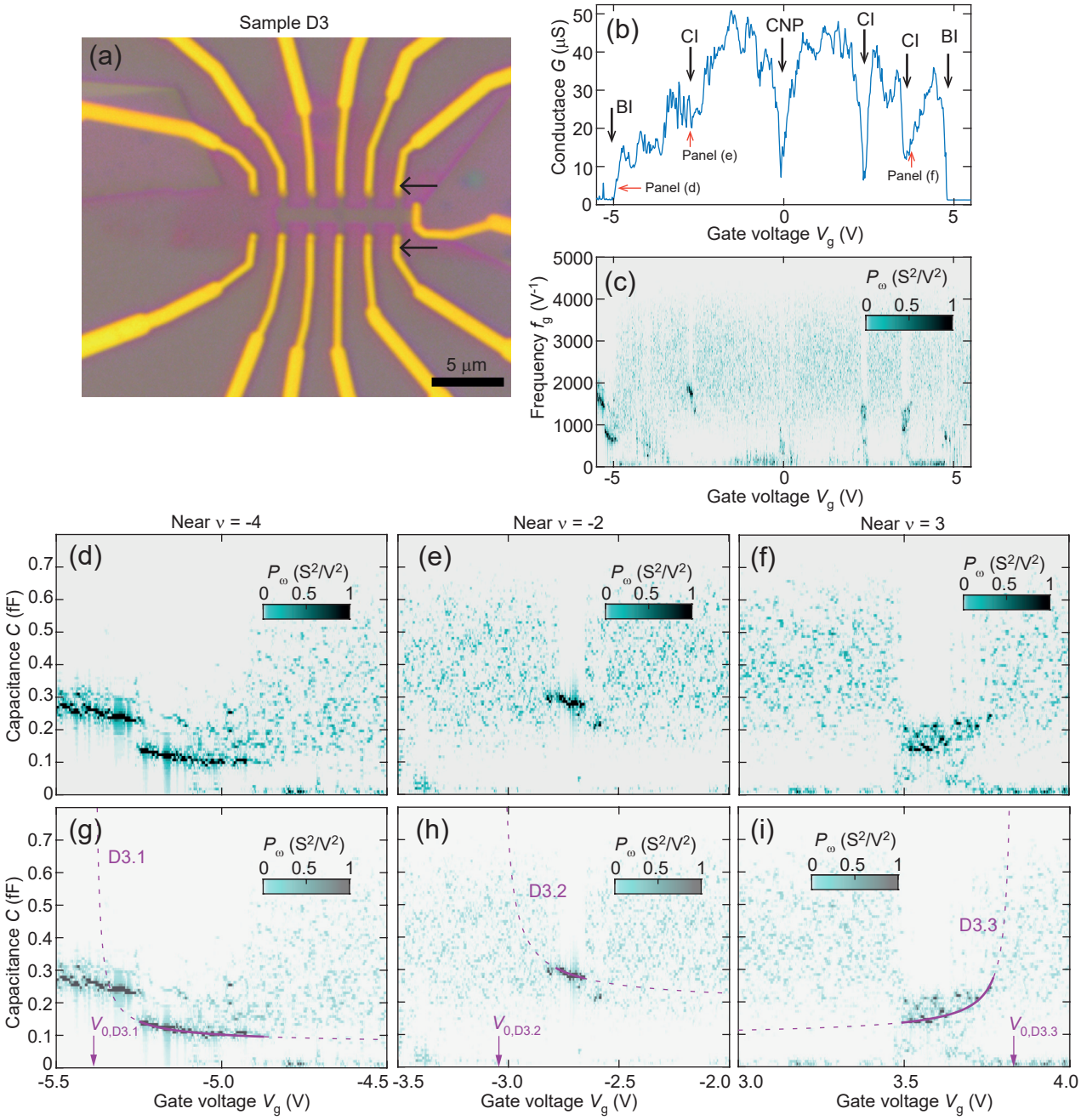

FIG. S8. Conductance oscillations observed in sample D3 with an estimated twist angle of 1.14°. (a) Optical image of the device, showing the two contacts used for 2-point characterization. (b) 2-point conductance as a function of gate voltage. The band insulator (BI), correlated insulators (CI) and charge neutrality point (CNP) are highlighted. (c) Power spectrum obtained from a 4-point measurement (the oscillations are more prominently visible due to oscillations of the contact resistance). (b) Zoom-in near the band insulator on the hole side and (g) fit to the frequency component. (e) Zoom-in near half-filling on the hole side and (h) fit to the component. (f) Zoom-in near 3/4 filling on the electron side and (i) fit to the frequency component.

TABLE S2. Summary of the fitting parameters for all frequency components with a fixed value of $S = 0.84$.

Component	Twist angle θ	Lever arm α (m^{-2} V^{-1})	Filling factor	Band	V_0 (V)	$\sqrt{A}$ (nm)	R^2
C1.1	1.02°	4.96×10^{15}	-4	Flat	-3.819 ± 0.003	333.3 ± 1.1	0.983
C1.2			-4	Flat	-3.536 ± 0.009	128.3 ± 0.9	0.911
C1.3		5.33×10^{15}	4	Flat	3.668 ± 0.004	308.3 ± 2.1	0.983
C1.4			4	Remote	3.771 ± 0.005	132.3 ± 2.4	0.929
C2.1	1.07°	4.96×10^{15}	-4	Remote	-4.265 ± 0.008	336.9 ± 1.3	0.958
C2.2			-4	Flat	-3.897 ± 0.012	301.7 ± 2.8	0.939
C2.3			-4	Flat	-3.845 ± 0.007	313.4 ± 3.7	0.980
C2.4		5.33×10^{15}	4	Flat	3.709 ± 0.006	269.3 ± 2.1	0.936
C2.5			4	Remote	3.759 ± 0.004	136.2 ± 2.1	0.940
C3.1	0.97°	4.96×10^{15}	-4	Remote	-4.219 ± 0.012	347.1 ± 2.7	0.947
C3.2			-4	Flat	-4.211 ± 0.005	325.3 ± 2.0	0.985
D2.1	0.97°	5.148×10^{15}	-4	Flat	-4.580 ± 0.002	142.6 ± 1.7	0.967
D2.2			-4	Flat	-3.945 ± 0.005	207.7 ± 1.8	0.943
D2.3			-4	Flat	-4.578 ± 0.009	336.5 ± 1.9	0.940
D2.4			2	Flat	2.671 ± 0.006	312.6 ± 0.8	0.976
D3.1	1.14°	5.509×10^{15}	-4	Flat	-5.444 ± 0.006	263.2 ± 1.1	0.945
D3.2			-2	Flat	-3.101 ± 0.015	430.6 ± 2.8	0.900
D3.3			3	Flat	3.889 ± 0.004	299.4 ± 1.8	0.952

S5. OBSERVATION OF CONDUCTANCE OSCILLATIONS NEAR $\nu = \pm 8$ IN A 0.65° TWISTED SAMPLE

In Fig. S9 we show conductance oscillations in sample D5. This sample has an estimated twist angle of 0.65°, where the insulating features appear at $\nu = \pm 8$ [8]. On both electron and hole side, we find an oscillating component with a low amplitude (note that the colorbar scale in Fig. S9(b) is lower than for the other power spectra presented in this work). It is clear that the frequency of these components increase as a function of gate voltage, and that their frequency increases when the Fermi level approaches $\nu = 8$. This may indicate that spatially correlated charge carriers are important in this system as well. We could, however, not obtain a good fit from Eq. (8). Possibly, this could indicate that the area A of the confinement is changing, or the interaction energy diminishes faster with increasing carrier density due to the smaller Wigner-Seitz radius.

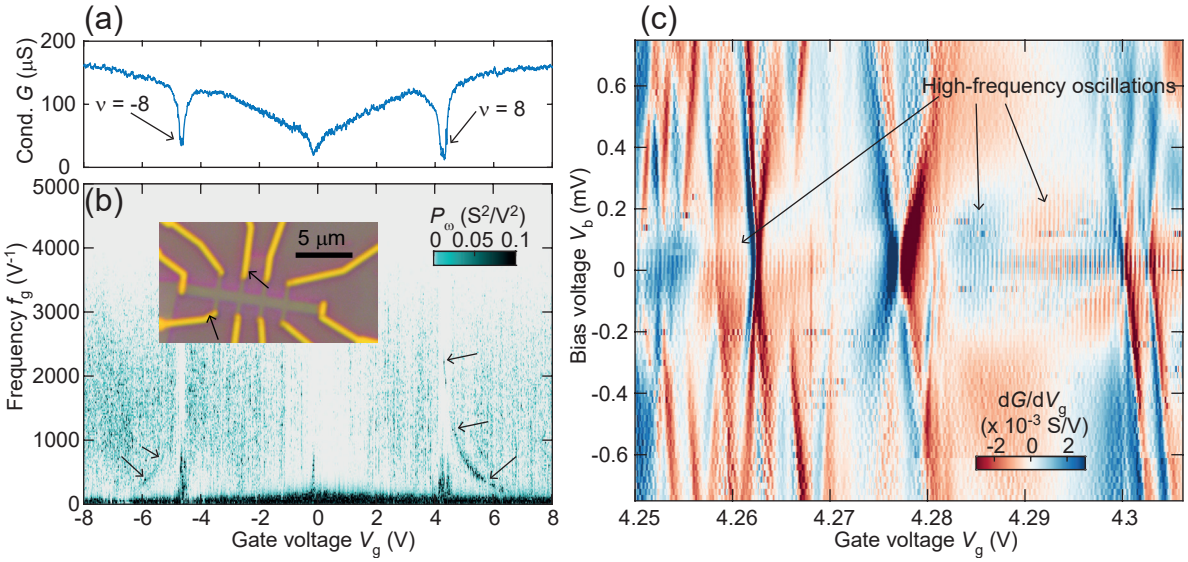

FIG. S9. Conductance oscillations observed in sample D5 with an estimated twist angle of 0.65°. (a) Two-point conductance as a function of gate voltage. At this twist angle, the insulating states are found near $\nu = 8$ [8], which we identify near $V_g = \pm 4.5$ V. (b) Power spectrum as a function of frequency and gate voltage: Note that the colour scale is a factor 10 lower than in all the other power spectra presented in this work. The inset shows an optical image of the device and the contacts used for 2-point characterization. (c) Bias-dependence of the gradient of the conductance. The typical Coulomb diamond structure is more difficult to discover due to the very high frequency and low amplitude, nevertheless the amplitude diminishes at roughly 0.2 mV, while the period of the high-frequency oscillation is 0.4 mV, which is consistent with Coulomb oscillations.

S6. COULOMB OSCILLATIONS IN A RELAXED SAMPLE

Figure S10(a) shows an optical image of device D6. During fabrication, this device was twisted at 1.3°, but the device relaxed back to Bernal stacking, which is evidenced by the absence of satellite peaks in Fig. S10(b). Furthermore, a top-gate was integrated in the device. An additional WSe_2 was incorporated into the stack, which breaks the inversion symmetry of the bilayer graphene and opens a bandgap. Despite the absence of moiré physics, we observe high-frequency Coulomb oscillations near the charge neutrality point [Figs. S10(c)-S10(d)]. Since the oscillations remain unchanged as a function of top-gate voltage, they likely emerge from a contact region that is only affected by the backgate [see Fig S10(a)]. Since the frequency, and therefore the charging energy, is similar in value to the frequency components in the main part of this work, this sample can serve as a control experiment. From Fig. S10(d), it is clear that the frequency remains constant as a function of gate voltage. This is in stark contrast to our observation on devices which show moiré satellite peaks, where the frequency increases at low carrier densities. This experiment therefore demonstrates that the band flattening in tBLG is crucial to observe a negative capacitance contribution.

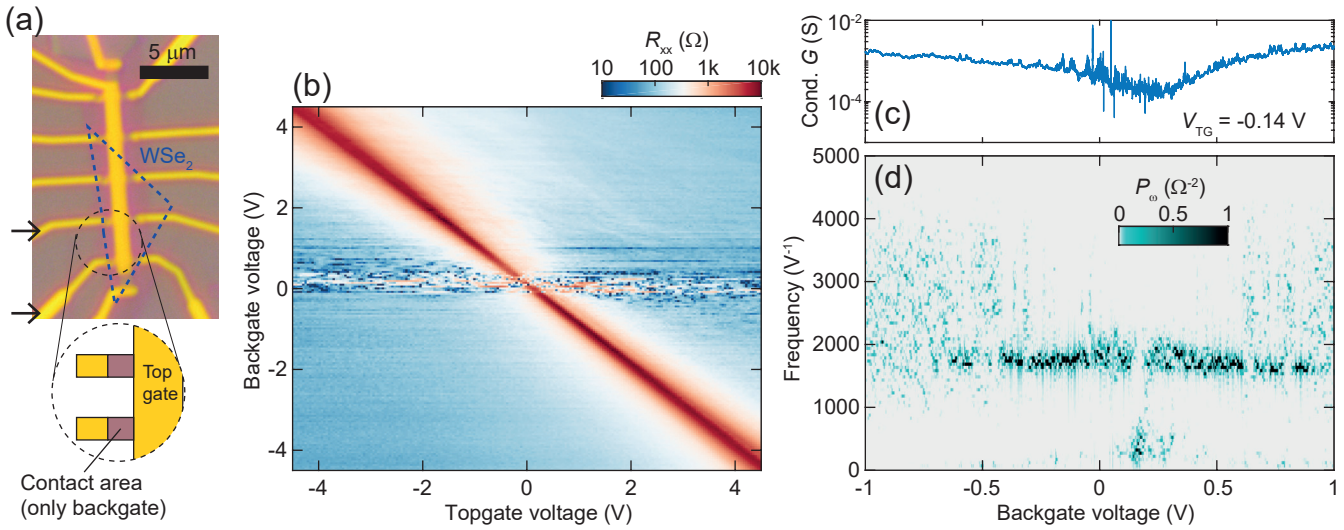

FIG. S10. Coulomb oscillations in a sample without moiré physics. (a) Optical image of device D6. The blue dotted line indicates the region where WSe_2 was incorporated into the stack. (b) 4-point resistance between the two contacts highlighted in panel (a) as a function of backgate and topgate voltage. (c) Two-point conductance as a function of backgate voltage at a fixed topgate voltage. (d) Power spectrum as a function of backgate voltage near the charge neutrality point.

S7. OBSERVATION OF COULOMB OSCILLATIONS IN SAMPLE D4

In Fig. S11(a) we show an atomic force microscopy map of sample D4, which consists of ring structures. Sample D4 showed significantly higher contact resistances than the other sample due to a different fabrication approach. Nevertheless, insulating states are resolved as shown in the 2-point conductance traces in Fig. S11(b). We observe insulating states that point to tBLG in three regions of the device. We estimate the twist angle from the hBN thickness (35.0 nm) and a parallel plate capacitor model, since the large contact resistances prevented us from making a more accurate estimation from magnetoresistance measurements.

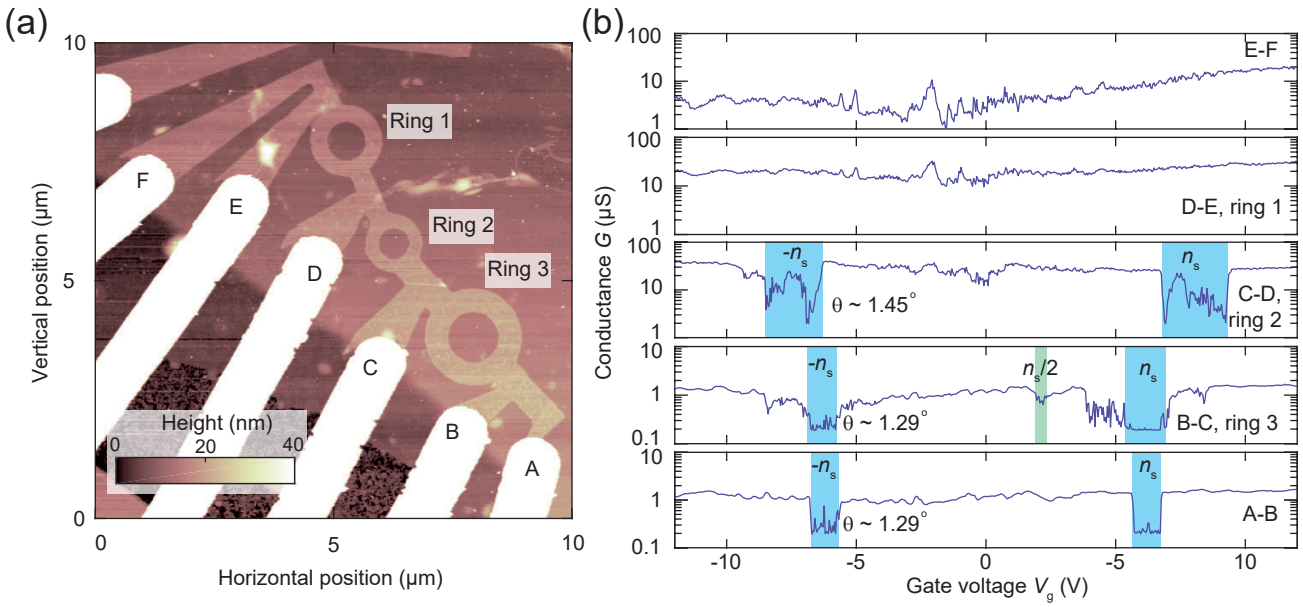

FIG. S11. 2-point conductance on sample D4. (a) Atomic force microscope image of sample D4, showing the tBLG sample in ring-shaped structures. (b) 2-point conductance measured between different contact pairs and the estimated twist angle.

In Fig. S12 we show the conductance oscillations observed in the 3 regions with insulating states. This sample also features Coulomb oscillations with perfect periodicity, suggesting that the charging energy also overcomes the quantum level spacing.

In sample D4 we were able to reproduce the magnetic field dependence of the oscillations, as outlined in the main text. In Fig. S13 we show that the phase of the oscillations tunes in an identical manner due to the quantum oscillation of the density of states in the region surrounding the confined region. In this case, we also find that the frequency is proportional to the gate voltage, which was also observed on constriction C1.

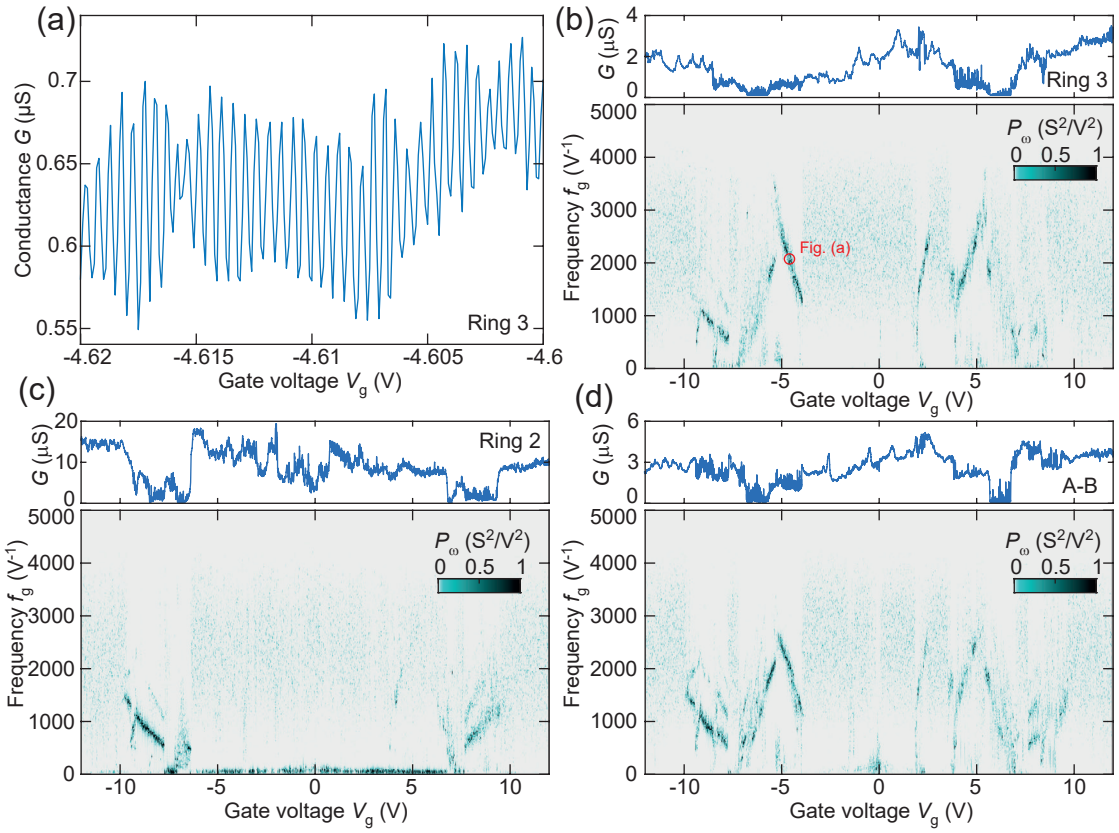

FIG. S12. Conductance oscillations observed in sample D4. (a) Conductance oscillations observed in an insulating state on Ring 3. (b) Power spectrum and conductance over the whole gate voltage range on Ring 3, (c) on Ring 2 and (d) on the section between contacts A-B.

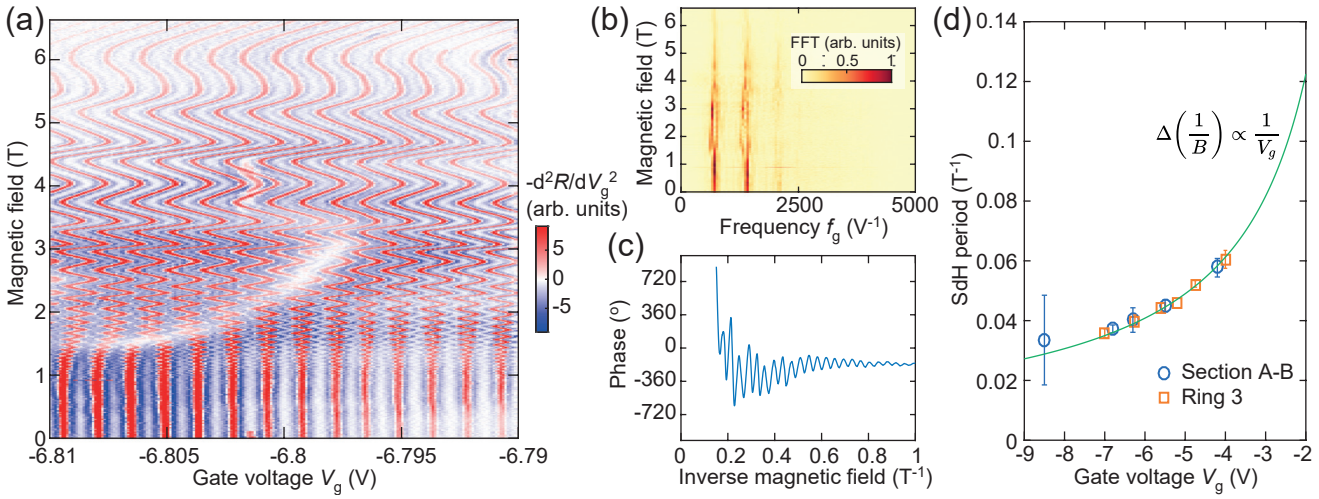

FIG. S13. Magnetic field dependence of the oscillations observed in sample D4. (a) Conductance oscillations as a function of magnetic field and gate voltage. (b) Power spectrum at each magnetic field, showing that the frequency of the oscillation remains unchanged. (c) Phase extracted from the power spectrum, showing that the oscillations are periodic in $1/B$. (d) Period of the oscillations as a function of gate voltage, showing that $\Delta\left(\frac{1}{B}\right) \propto \frac{1}{V_g}$.

S8. COULOMB OSCILLATIONS IN REVERSED MAGNETIC FIELD

Figs. S14(a)–S14(d) present Coulomb blockade oscillations obtained from device D4, specifically from the section labeled "Ring 3". In this instance, the twist angle deviates somewhat from the magic angle, estimated at 1.29°, and the frequency components do not align well with Eq. 5. Nonetheless, the noticeable increase in frequency as we approach the insulating states hints at a considerable negative contribution to capacitance even in this scenario (Fig. S12). Examining the frequency content of the signal in Figs. S14(e)–S14(f), we observe no significant alteration in oscillation frequency concerning changes in the magnetic field or when reversing the magnetic field direction.

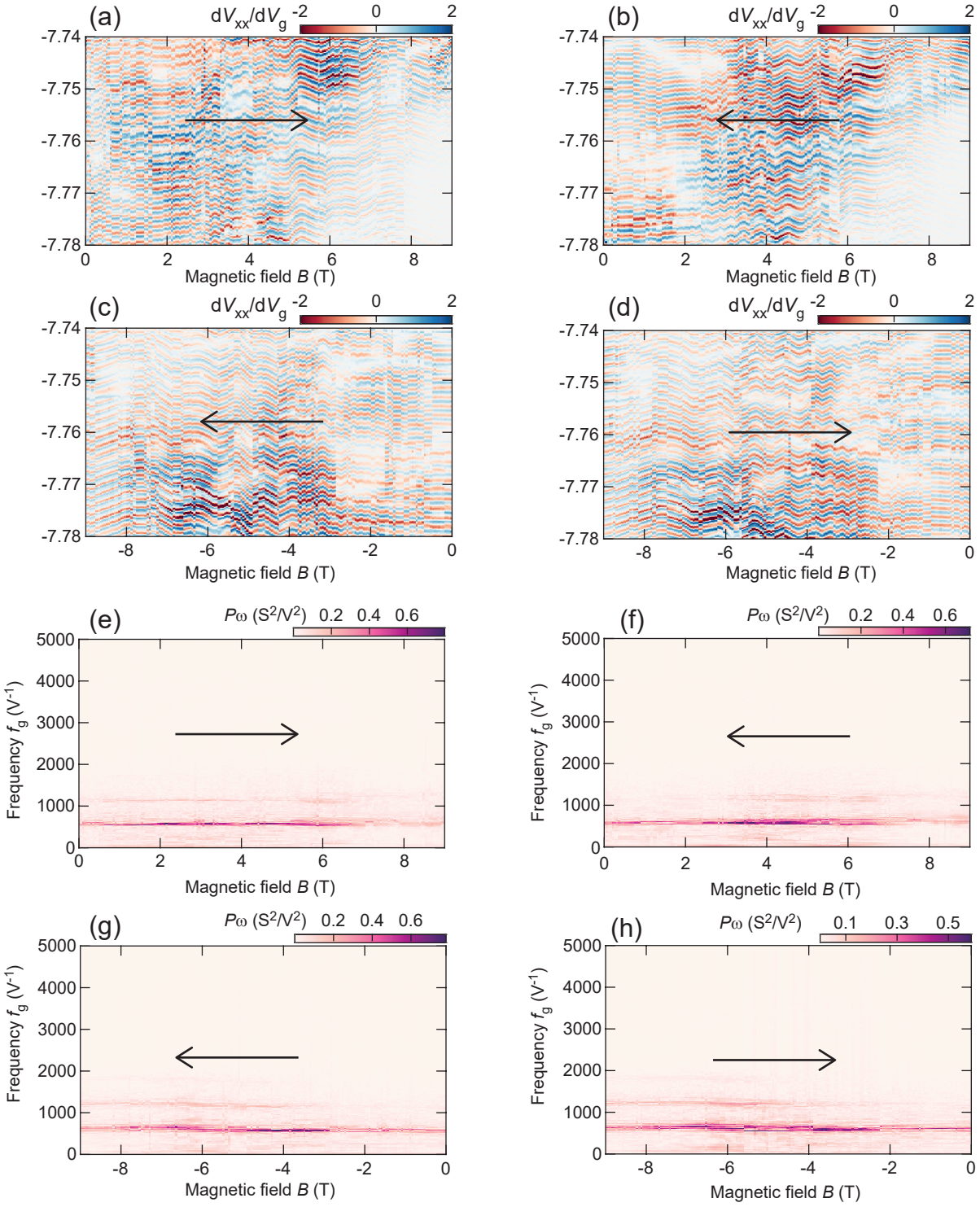

FIG. S14. Coulomb oscillations as a function of magnetic field in sample D4. (a–d) Gradient of the voltage drop as a function of magnetic field, sweeping from: (a) 0 T to 9 T, (b) 9 T to 0 T, (c) 0 to -9 T and (d) -9 T to 0 T. (e–h) Frequency content of the oscillations, sweeping the magnetic field from: (e) 0 T to 9 T, (f) 9 T to 0 T, (g) 0 to -9 T and (h) -9 T to 0 T.

S9. MAGNETIC FIELD DEPENDENCE OF THE NEGATIVE CAPACITANCE CONTRIBUTION

In this section we present a more detailed investigation of the Coulomb oscillations associated with the frequency component C1.3 under the influence of an out-of-plane magnetic field. In Fig. S15(a), S15(c), and S15(e), we sweep the gate voltage within a narrow range around specific values [V_g = 3.4 V, 3.52 V, and 3.161 V as indicated in Fig. 2(f)] while incrementally increasing the magnetic field. Once again, we clearly observe quantum oscillations, evident as shifts in peak positions. Furthermore, the separation between the peaks, corresponding to the frequency of the Coulomb oscillations, remains entirely consistent despite the increase in magnetic field strength. This stability is further affirmed by the power spectra depicted in Figs. S15(b), S15(d), and S15(f), where the frequency component C1.3 is clearly identifiable in each spectrum (indicated by an arrow). It is important to note that while the amplitude of the oscillations may vary, we do not observe a continuous shift in the frequency, which would suggest a change in the polarization of the electron gas. Instead, frequency components appear or disappear as a function of the magnetic field. This phenomenon can be attributed to multiple charge island being present on the samples, wherein the prominence of the Coulomb blockade changes with the magnetic field. However, in Fig. S15(b) and S15(f), the component C1.3 appears both at 0 T and 9 T, demonstrating that the frequency of an individual charge island remains constant.

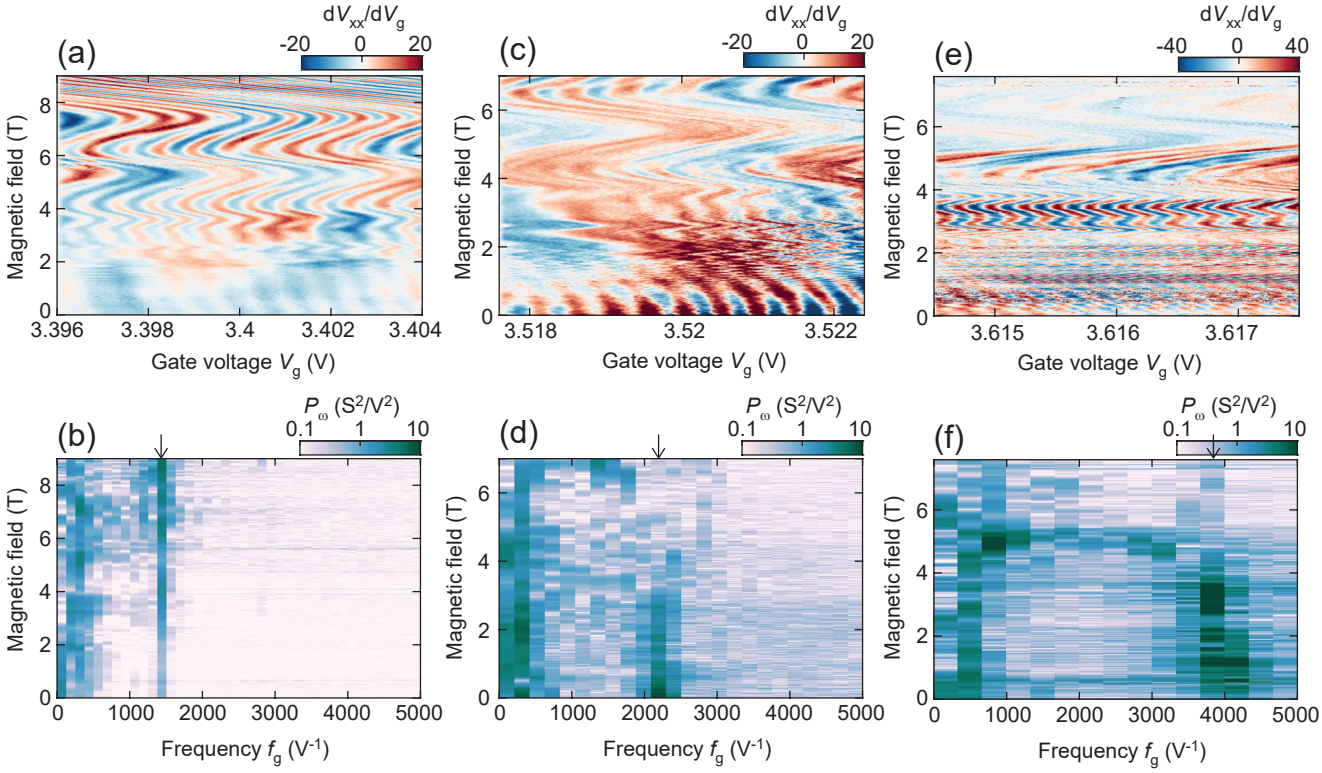

FIG. S15. (a,c,e) Coulomb oscillations as a function of magnetic field near V_g = 3.4 V, V_g = 3.52 V and V_g = 3.616 V, respectively. (b,d,f) Fast-Fourier-transform of the oscillations as a function of magnetic field near V_g = 3.4 V, V_g = 3.52 V and V_g = 3.616 V, respectively.

[1] J. M. Park, Y. Cao, L.-Q. Xia, S. Sun, K. Watanabe, T. Taniguchi, and P. Jarillo-Herrero, Robust Superconductivity in Magic-Angle Multilayer Graphene Family, Nat. Mater. **21**, 877 (2022).
[2] K. P. Nuckolls, M. Oh, D. Wong, B. Lian, K. Watanabe, T. Taniguchi, B. A. Bernevig, and A. Yazdani, Strongly Correlated Chern Insulators in Magic-Angle Twisted Bilayer Graphene, Nature **588**, 610 (2020).
[3] S. L. Tomarken, Y. Cao, A. Demir, K. Watanabe, T. Taniguchi, P. Jarillo-Herrero, and R. C. Ashoori, Electronic Compressibility of Magic-Angle Graphene Superlattices, Phys. Rev. Lett. **123**, 046601 (2019).
[4] P. Stepanov, M. Xie, T. Taniguchi, K. Watanabe, X. Lu, A. H. MacDonald, B. A. Bernevig, and D. K. Efetov, Competing Zero-Field Chern Insulators in Superconducting Twisted Bilayer Graphene, Phys. Rev. Lett. **127**, 197701 (2021).
[5] Y. Saito, J. Ge, L. Rademaker, K. Watanabe, T. Taniguchi, D. A. Abanin, and A. F. Young, Hofstadter Subband ferromagnetism and Symmetry-Broken Chern insulators in Twisted Bilayer Graphene, Nat. Phys. **17**, 478 (2021).
[6] S. Wu, Z. Zhang, K. Watanabe, T. Taniguchi, and E. Y. Andrei, Chern Insulators, van Hove Singularities and Topological Flat Bands in Magic-Angle twisted Bilayer Graphene, Nat. Mater. **20**, 488 (2021).
[7] J. M. Park, Y. Cao, K. Watanabe, T. Taniguchi, and P. Jarillo-Herrero, Flavour Hund's Coupling, Chern Gaps and Charge Diffusivity in Moiré Graphene, Nature **592**, 43 (2021).
[8] Y. Cao, V. Fatemi, A. Demir, S. Fang, S. L. Tomarken, J. Y. Luo, J. D. Sanchez-Yamagishi, K. Watanabe, T. Taniguchi, E. Kaxiras, R. C. Ashoori, and P. Jarillo-Herrero, Correlated Insulator Behaviour at Half-Filling in Magic-Angle Graphene Superlattices, Nature **556**, 80 (2018).